

Optical nonlocality in multilayered hyperbolic metamaterials based on Thue-Morse superlattices

Silvio Savoia, Giuseppe Castaldi, and Vincenzo Galdi*

Waves Group, Department of Engineering, University of Sannio, I-82100 Benevento, Italy

(Received 30 November 2012; revised manuscript received 27 May 2013; published 12 June 2013)

We show that hyperbolic electromagnetic metamaterials, implemented as multilayers based on two material constituents arranged according to the Thue-Morse aperiodic sequence, may exhibit strong nonlocal effects, manifested as the appearance of additional extraordinary waves which are not predicted by standard effective-medium-theory (local) models. From the mathematical viewpoint, these effects can be associated with stationary points of the transfer-matrix trace and can be effectively parametrized via the trace-map formalism. We show that their onset is accompanied by a strong wave-vector dependence in the effective constitutive parameters. Despite the inherent periodicity enforced by the unavoidable (Bloch-type) supercell terminations, we show that such strong nonlocality is retained at any arbitrarily high-order iteration, i.e., approaching the actual aperiodic regime. Moreover, for certain parameter configurations, at a given wavelength and for two given material layers, these effects may be significantly less prominent when the same layers are arranged in a standard periodic fashion. Our findings indicate that the (aperiodic) positional order of the layers constitutes an effective and technologically inexpensive additional degree of freedom in the engineering of optical nonlocality.

DOI: [10.1103/PhysRevB.87.235116](https://doi.org/10.1103/PhysRevB.87.235116)

PACS number(s): 42.25.Bs, 61.44.Br, 78.20.Ci, 78.67.Pt

I. INTRODUCTION

Electromagnetic (EM) metamaterials are artificial materials composed of subwavelength dielectric and/or metallic inclusions in a host medium, which have attracted considerable scientific and application-oriented attention due to the possibility to engineer anomalous properties (e.g., negative refraction) that are not observable in natural materials.¹ Of particular interest are the so-called “hyperbolic” metamaterials,^{2,3} characterized by nonmagnetic uniaxially anisotropic constitutive relationships with both positive and negative components of the permittivity tensor. This yields a *hyperbolic* (as opposed to *spherical* in conventional isotropic media) dispersion relationship, which allows for the propagation of (otherwise evanescent) waves with large wave vectors, resulting in a high (theoretically unbounded) photonic density of states. The reader is referred to Refs. 4–12 for a sparse sampling of applications, ranging from nanoimaging to quantum nanophotonics and thermal emission.

In what follows, we focus on multilayered hyperbolic metamaterials,⁷ implemented via the stacking of alternating subwavelength layers with negative and positive permittivities (e.g., metallic and dielectric at optical wavelengths). For this class, the effective-medium theory (EMT) provides a particularly simple model in terms of a homogeneous uniaxially anisotropic permittivity tensor with components given by the Maxwell-Garnett mixing formulas.¹³ However, a series of recent papers^{14–18} have pointed out the limitations of this model in predicting *nonlocal* effects that can take place (even in the presence of deep subwavelength layers) due to the coupling of surface-plasmon polaritons (SPPs) propagating along the interfaces separating layers with oppositely signed permittivities. This may result, for instance, in the misprediction of additional extraordinary waves^{15,18} as well as of the broadband Purcell effect.¹⁷

We point out that typical multilayered hyperbolic metamaterials are based on *periodic* arrangements of the layers.⁷ In fact, the EMT model describing the *local* response is independent of the positional order of the layers and depends

only on the permittivities of the two constituents and their filling fractions.¹³ However, one would intuitively expect the positional order of the layers to sensibly affect the *nonlocal* response. It seems, therefore, suggestive to investigate possible nonlocal effects in structures characterized by *aperiodic order* inspired by the “quasicrystal” concept in solid-state physics.^{19,20}

Within this framework, here, we study the nonlocal response of hyperbolic metamaterials constituted by multilayer superlattices based on the Thue-Morse (ThM) geometry.²¹ For these structures, we identify certain nonlocal effects in terms of additional extraordinary waves, that are strongly dependent on the specific positional order of the material layers. Accordingly, the rest of the paper is laid out as follows. In Sec. II, we introduce the problem geometry and formulation as well as the main analytical tools utilized (with details relegated in Appendices A and B). In Sec. III, we derive, illustrate, and validate the main results, via analytical studies, retrieval of effective wave-vector-dependent constitutive parameters, and full-wave numerical simulations. In Secs. IV and V, we provide some additional remarks and conclusions, respectively.

II. PROBLEM FORMULATION AND ANALYTICAL MODELING

A. Problem geometry and generalities

Referring to the two-dimensional (2D) y -independent geometry in Fig. 1, we consider a multilayer superlattice obtained via the infinite repetition along the z axis of a supercell composed of layers of two nonmagnetic material constituents labeled with the letters “ a ” and “ b ” (with relative permittivities ε_a and ε_b and thicknesses d_a and d_b , respectively), arranged according to the ThM sequence. Assuming the sequence “ ab ” as an initiator, this amounts to iterating the following inflation rules:²¹

$$a \rightarrow ab, \quad b \rightarrow ba, \quad (1)$$

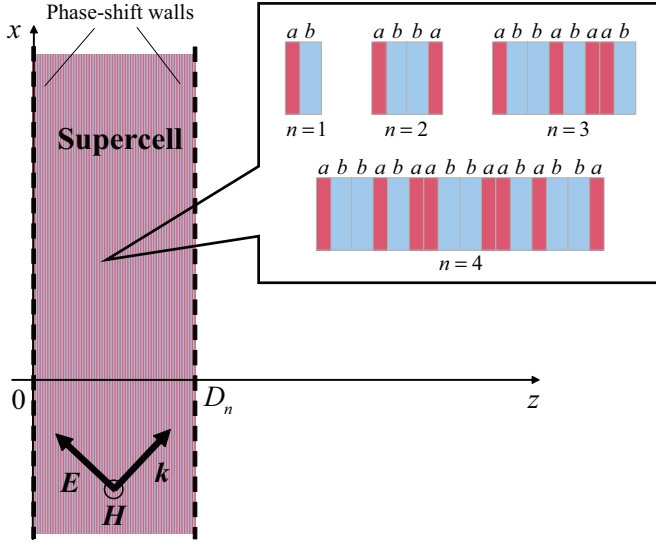


FIG. 1. (Color online) Problem schematic, illustrating the 2D propagation of TM-polarized EM fields (with a y -directed magnetic field) in the ThM-based hyperbolic metamaterial of interest (details in the text).

as shown schematically in the inset of Fig. 1 for the first iteration orders n . In what follows, we study the time-harmonic $[\exp(-i\omega t)]$ propagation of transverse-magnetic (TM-) polarized EM fields neglecting, for now, material losses as previous studies¹⁸ have shown that they only mildly affect optical nonlocality.

It is readily recognized that the first two iterations ($n = 1, 2$) correspond to standard periodic multilayers (with periods $d = d_a + d_b$ and $2d$, respectively); these will be accordingly referred to as the “standard periodic” cases. In fact, we emphasize that the geometry in Fig. 1 is *inherently periodic* for any finite iteration order n and approaches the actual aperiodic regime in the limit $n \rightarrow \infty$ (see Sec. IV A below). Moreover, we observe that, given the structure of the inflation rule in (1), any iteration order of our ThM multilayer contains the same proportions of a -type and b -type constituents as the standard periodic case and differs solely in the positional order of the layers. Accordingly, the Maxwell-Garnett mixing formulas for the parallel (\parallel , i.e., x, y) and orthogonal (\perp , i.e., z) permittivity components,¹³

$$\varepsilon_{\parallel} = \frac{\varepsilon_a d_a + \varepsilon_b d_b}{d}, \quad \varepsilon_{\perp} = \left(\frac{\varepsilon_a^{-1} d_a + \varepsilon_b^{-1} d_b}{d} \right)^{-1} \quad (2)$$

yield the same EMT model for any iteration order, which results in the dispersion relationship,

$$\frac{k_x^2}{\varepsilon_{\perp}} + \frac{k_z^2}{\varepsilon_{\parallel}} = k^2, \quad (3)$$

where k_x and k_z indicate the x and z components, respectively, of the wave vector \mathbf{k} (cf. Fig. 1) and $k = \omega/c = 2\pi/\lambda$ indicates the vacuum wave number (with c and λ denoting the corresponding wave speed and wavelength). By suitably choosing the parameters in the mixing rules (2) so that $\varepsilon_{\parallel}\varepsilon_{\perp} < 0$, the dispersion relationship in (3), interpreted in terms of the *equifrequency contour* (EFC), assumes the anticipated *hyperbolic* character. Since the local EMT model in (2) and (3)

is *identical* for any iteration order, any possible difference in the (nonlocal) responses should solely be attributed to the different positional orders of the material layers.

B. Exact dispersion relationship

Multilayers based on the ThM geometry have been widely studied in the past in the form of dielectric/semiconductor photonic quasicrystals (see, e.g., Refs. 22–27 for a sparse sampling) and with the main focus on the resonant-transmission, localization, omnidirectional-reflection, and band-gap properties. Against this background, ThM-based hyperbolic metamaterials are studied here. Following a rather standard approach (see Appendix A for more details), the *exact* dispersion relationship pertaining to a n th-order ThM supercell terminated by Bloch-type phase-shift walls (cf. Fig. 1) can be compactly written as

$$\cos(k_z D_n) = \frac{\chi_n}{2}, \quad (4)$$

where $D_n = 2^{n-1}d$ represents the total supercell thickness at the iteration order n and χ_n denotes the *trace* (i.e., the sum of the diagonal elements) of the transfer matrix that relates the tangential components of the EM fields at the supercell interfaces $z = 0$ and $z = D_n$. For the first two iterations $n = 1, 2$, the trace can be straightforwardly calculated as

$$\chi_n = 2 \cos(n\delta_a) \cos(n\delta_b) - \left(\frac{\gamma_a}{\gamma_b} + \frac{\gamma_b}{\gamma_a} \right) \sin(n\delta_a) \sin(n\delta_b), \quad (5)$$

thereby recovering the familiar Bloch-type dispersion relationship of the standard periodic multilayers (as in Refs. 14–18) where

$$\delta_{a,b} = k_{za,b} d_{a,b}, \quad \gamma_{a,b} = \frac{\varepsilon_{a,b} k}{k_{za,b}}, \quad (6)$$

with $k_{za,b} = \sqrt{k^2 \varepsilon_{a,b} - k_x^2}$, $\text{Im}(k_{za,b}) \geq 0$. For higher-order iterations, a particularly simple recursive calculation procedure can be adopted, based on the *trace map*^{28,29} (see also Appendix B for details),

$$\chi_{n+2} = \chi_n^2 (\chi_{n+1} - 2) + 2, \quad n \geq 1. \quad (7)$$

C. Conditions for additional extraordinary waves

The exact dispersion relationship in (4) reduces to the local EMT model in (3) in the limit $d \rightarrow 0$, but it may significantly depart from that for finite (and yet subwavelength) layer thicknesses. In particular, we are interested in exploring possible nonlocal effects manifested as the appearance of additional extraordinary waves that are not predicted by the local EMT model in (3) and have already been observed in hyperbolic metamaterials based on standard periodic multilayers.^{15,18} From the mathematical viewpoint, this phenomenon is related to *multiple* (apart from the sign) k_x solutions of (4) for given values of k_z and ω , which may occur if the trace χ_n is a *nonmonotonic* function of k_x^2 . We are, therefore, led to study the *stationary points* of the trace χ_n with respect to the argument k_x^2 ,

$$\dot{\chi}_n(k_x^2) = 0. \quad (8)$$

III. REPRESENTATIVE RESULTS

A. Trace-map and EFC studies

In order to better emphasize the role of the positional order in the onset of these nonlocal phenomena, we deliberately focus on parameter configurations for which the hyperbolic metamaterial arising from the first iteration $n = 1$ (i.e., a standard periodic multilayer) is well described by the local EMT model in (3). This translates in the trace χ_1 in (5) being well approximated by its second-order Taylor expansion in d ,

$$\chi_1(k_x^2) \approx 2 - \varepsilon_{\parallel} k^2 d^2 + \frac{\varepsilon_{\parallel} d^2}{\varepsilon_{\perp}} k_x^2. \quad (9)$$

Figure 2(a) compares, for one such parameter configuration (given in the caption and corresponding to $\varepsilon_{\parallel} = 2.5$ and $\varepsilon_{\perp} = -5$), the exact trace χ_1 [cf. (5)] and its quadratic approximation (9), showing a reasonable agreement. The corresponding exact [cf. (4)] EFCs and the local-EMT prediction [cf. (3)] are compared in Fig. 2(b) within the first Brillouin zone $0 \leq k_z \leq \pi/d$. Again, we observe good agreement (especially for smaller values of k_z) and, most importantly, a *single* branch. This yields a *single* mode that is propagating for $k_z \gtrsim \sqrt{\varepsilon_{\parallel}} k \approx 0.32\pi/d$ and is evanescent otherwise. We now move on to looking at higher-order iterations of the ThM geometry. From the trace map in (7), we straightforwardly obtain

$$\dot{\chi}_{n+2} = \chi_n [\chi_n \dot{\chi}_{n+1} + 2\dot{\chi}_n (\chi_{n+1} - 2)], \quad n \geq 1, \quad (10)$$

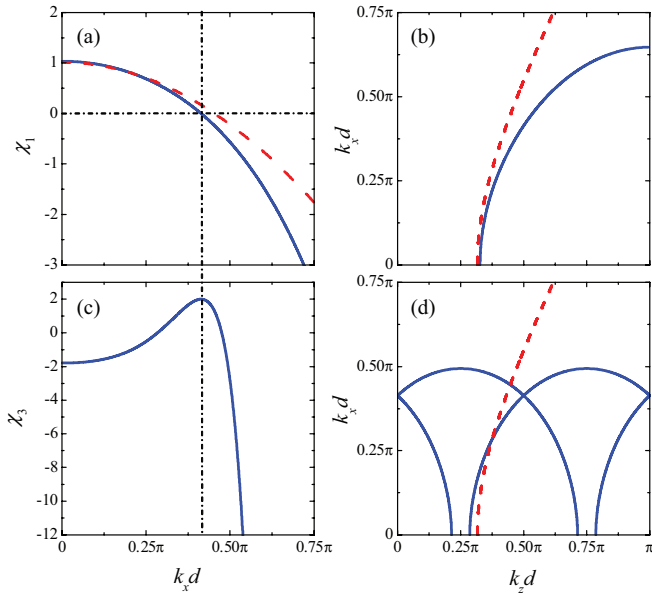


FIG. 2. (Color online) (a) Transfer-matrix trace (blue-solid curve) as a function of k_x and (b) corresponding EFC (within the first Brillouin zone) for a hyperbolic metamaterial with $\varepsilon_a = 6.83$, $\varepsilon_b = -1.83$, and $d_a = d_b = d/2 = 0.05\lambda$ (i.e., $\varepsilon_{\parallel} = 2.5$, $\varepsilon_{\perp} = -5$) at the $n = 1$ iteration order (i.e., standard periodic multilayer of period d). Also shown (red-dashed curves) are the predictions from the local EMT model. Due to symmetry, only positive values of k_x and k_z are shown. (c) and (d) Same as above but for the $n = 3$ iteration order (four Brillouin zones shown for direct comparison). The dashed-dotted lines highlight the correspondence between the zero of χ_1 and the maximum of χ_3 .

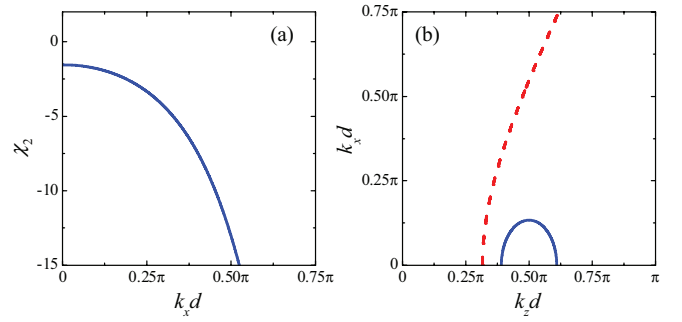


FIG. 3. (Color online) As in Figs. 2(a) and 2(b) but for the $n = 2$ iteration order (standard periodic multilayer of period $2d$; two Brillouin zones shown in the EFCs).

with the overdot denoting differentiation with respect to the argument k_x^2 . This implies that the vanishing of the trace at a given iteration order, i.e., $\chi_n = 0$, is a sufficient condition for a stationary point $\dot{\chi}_{n+2} = 0$ and, hence, the presence of additional extraordinary waves at a higher-order iteration. Therefore, if the trace χ_1 admits a zero, then χ_3 should exhibit, at least, one stationary point. For the assumed parameter configuration, for which the local EMT model and, hence, the quadratic approximation in (9) holds reasonably well at the first iteration order, the position k_{x0} of such a zero (and corresponding stationary point) admits a simple analytical estimate as

$$k_{x0} \approx \frac{1}{d} \sqrt{\frac{\varepsilon_{\perp}(\varepsilon_{\parallel} k^2 d^2 - 2)}{\varepsilon_{\parallel}}}, \quad (11)$$

which yields a real solution provided that $\varepsilon_{\parallel} k^2 d^2 \leq 2$. In our case, this last condition is verified, and, as can be observed from Fig. 2(a), the estimate in (11) is moderately accurate, yielding a 9% error with respect to the actual zero position $k_{x0} = 0.4138d/\pi$ calculated numerically. For the same parameter configuration, Fig. 2(c) shows the trace χ_3 at the $n = 3$ iteration order from which a maximum at k_{x0} can be observed. As a consequence, besides a branch that is still in good agreement with the local EMT prediction, the corresponding EFCs shown in Fig. 2(d) [within a spectral region covering four Brillouin zones in order to facilitate direct comparison with Fig. 2(b)] exhibit additional branches, resulting in two additional modes (extraordinary waves) that propagate for arbitrarily small values of k_z and degenerate into a single mode at $k_z^{(m)} = m\pi/(2d)$, $m = 0, 1, 2, \dots$.

Figures 3–5 illustrate the results pertaining to the intermediate ($n = 2$) and higher ($n = 4$ and $n = 5$) iteration orders, respectively. More specifically, the $n = 2$ iteration order illustrated in Fig. 3 still corresponds to a standard periodic multilayer (of period $2d$). For the chosen parameter configuration, the local EMT prediction is less accurate than what is observed for the case [cf. Figs. 2(a) and 2(b)] but still correctly predicts a single mode that is evanescent below a cutoff value of k_z . Likewise, looking at the results for the $n = 4$ iteration order in Fig. 4, we note that the trace χ_4 exhibits a maximum ($\chi_4 = 2$) at k_{x0} . We, therefore, obtain two (always propagating) modes which degenerate at $k_z^{(m)} = m\pi/(4d)$, $m = 0, 1, 2, \dots$. This is qualitatively similar to what is observed for the $n = 3$ case [cf. Figs. 2(c) and 2(d)],

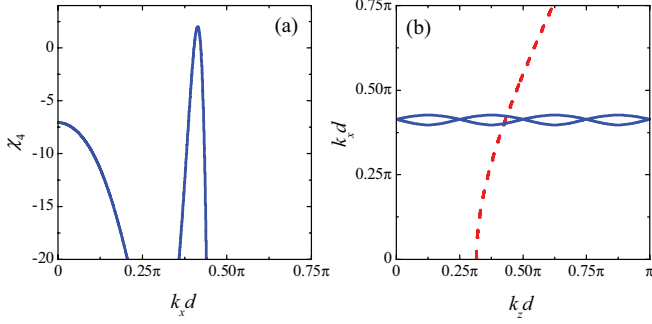


FIG. 4. (Color online) As in Figs. 2(a) and 2(b) but for the $n = 4$ iteration order (eight Brillouin zones shown in the EFCs).

although now, both modes turn out to depart substantially from the local EMT prediction. Rather differently, and quite interesting, are the results pertaining to the $n = 5$ iteration order. As can be observed from Fig. 5(a), the trace χ_5 now exhibits *three* maxima ($\chi_5 = 2$). In the corresponding EFCs [Fig. 5(b)], this translates into *six* (always propagating) modes which degenerate at $k_z^{(m)} = m\pi/(8d), m = 0, 1, 2, \dots$

B. Nonlocal effective constitutive parameters

An effective nonlocal model capable of capturing the above effects can be derived in terms of a homogeneous uniaxial medium with *wave-vector-dependent* relative-permittivity components $\hat{\epsilon}_{\parallel}(\mathbf{k})$ and $\hat{\epsilon}_{\perp}(\mathbf{k})$, whose dispersion law,

$$\frac{k_x^2}{\hat{\epsilon}_{\parallel}(\mathbf{k})} + \frac{k_z^2}{\hat{\epsilon}_{\perp}(\mathbf{k})} = k^2 \quad (12)$$

suitably approximates the exact dispersion law in (4). In Ref. 14, for a similar (standard periodic multilayer) configuration, such a model was successfully derived in terms of second-order rational functions (of k_x and k_z) so that the exact and approximate dispersion laws would match up to the fourth order in d . In our case here, in view of the generally larger dynamical ranges observed, we found it necessary to derive a higher-order model,

$$\hat{\epsilon}_{\parallel}(k_x) = \frac{1}{\alpha_0 + \alpha_2 k_x^2 + \alpha_4 k_x^4 + \alpha_6 k_x^6 + \alpha_8 k_x^8}, \quad (13a)$$

$$\hat{\epsilon}_{\perp}(k_z) = \frac{1}{\beta_0 + \beta_2 k_z^2 + \beta_4 k_z^4 + \beta_6 k_z^6 + \beta_8 k_z^8}, \quad (13b)$$

by matching the exact dispersion law in (4) up to the tenth order in d . The coefficients α_l and $\beta_l, l = 0, 2, 4, 6, 8$, generally depend on the frequency and on the geometrical and constitutive parameters of the multilayer and are given in Tables I and II, respectively, for the parameter configuration and iteration orders ($n = 1$ and $n = 3$) as in Fig. 2.

TABLE I. Geometry and parameters as in Fig. 2. Coefficients $\alpha_l, l = 0, 2, 4, 6, 8$, pertaining to the effective nonlocal relative permittivity $\hat{\epsilon}_{\parallel}(k_x)$ in (13a) for the $n = 1$ and $n = 3$ iteration orders.

n	α_0	α_2	α_4	α_6	α_8
1	0.409	$-0.034d^2$	$1.136 \times 10^{-3}d^4$	$-2.028 \times 10^{-5}d^6$	$2.254 \times 10^{-7}d^8$
3	1.670	$-2.227d^2$	$1.188d^4$	$-0.339d^6$	$0.060d^8$

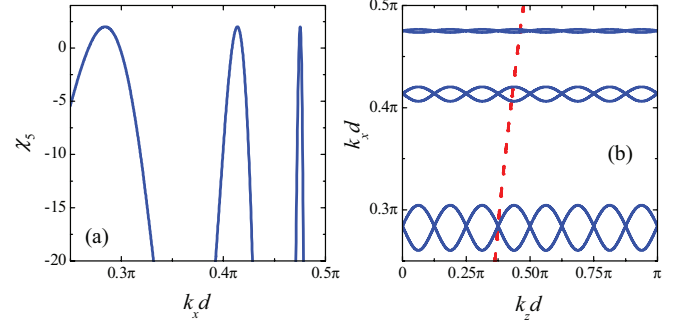


FIG. 5. (Color online) As in Figs. 2(a) and 2(b) but for the $n = 5$ iteration order (16 Brillouin zones shown in the EFCs).

As can be expected, for the $n = 1$ iteration order (standard periodic multilayer), the coefficients pertaining to higher-order terms in k_x and k_z are quite small. The resulting mild wave-vector dependence in the effective parameters is also visible in Figs. 6(a) and 6(b), whereas, Fig. 6(c) shows the excellent agreement between the exact EFC and the prediction from the nonlocal effective model.

Conversely, for the $n = 3$ iteration order, these higher-order coefficients are *non-negligible*, thereby confirming the quite strong wave-vector dependence in the effective constitutive parameters as evidently visible in Figs. 7(a) and 7(b). Overall, as shown in Fig. 7(c), the nonlocal effective model is capable of accurately capturing (over the first Brillouin zone) the peculiar multibranch behavior of the EFCs.

It should be stressed that the above approach is not the only one available (see, e.g., Ref. 16 for an alternative) and that it is inherently limited to the modal analysis in a *bulk*-medium scenario. Applications to boundary-value problems generally require more refined models as well as the derivation of additional boundary conditions.³⁰

C. Propagation through a slab

We now focus on an independent validation of our findings above. To this aim, for computational affordability, we study the TM plane-wave propagation through a slab of our ThM-based hyperbolic metamaterial (infinitely long in the z direction and of finite thickness along x with parameters as in Fig. 2) immersed in vacuum at various iteration orders. Our numerical simulations below rely on a rigorous coupled wave analysis algorithm,³¹ based on the Fourier-series expansion of the piecewise-constant permittivity distribution of the supercell. In our study, the truncation of this expansion was chosen according to a convergence criterion based on the root-mean-square (RMS) variations in the magnetic-field distribution within the supercell. Basically, the number of

TABLE II. As in Table I but coefficients $\beta_l, l = 0, 2, 4, 6, 8$, pertaining to $\hat{\epsilon}_\perp(k_z)$ in (13b).

n	β_0	β_2	β_4	β_6	β_8
1	-0.220	$-0.017d^2$	$5.58 \times 10^{-4}d^4$	$-9.921 \times 10^{-6}d^6$	$-1.127 \times 10^{-7}d^8$
3	0.138	$0.134d^2$	$-8.263 \times 10^{-3}d^4$	$-0.017d^6$	$-2.71 \times 10^{-3}d^8$

modes in the expansion was increased until RMS variations $< 2\%$ were observed. For the larger supercells considered in our study ($n = 5$ iteration order, i.e., 32 layers), convergence was achieved by using 391 modes.

Figure 8(a) shows a field-magnitude map pertaining to the first iteration order $n = 1$ (i.e., standard periodic multilayer) for normal incidence ($k_z = 0$) and thickness $L = 0.75\lambda$. As can also be observed from the longitudinal (x) cut in Fig. 8(b), the field is totally reflected with only an evanescent decay inside the slab, which is accurately fitted by an exponential tail (red-dashed curve) with attenuation coefficient,

$$\alpha_x \approx \sqrt{|\epsilon_\perp|}k, \quad (14)$$

as predicted by the local EMT model in (3). The z cut in Fig. 8(c) shows that the transverse field distribution is rather uniform ($\sim 10\%$ variations) and weakly peaked at the centers of the layers. Overall, as expected, the local EMT model provides a satisfactory prediction. Similar considerations hold for the $n = 2$ iteration order (standard periodic multilayer of period $2d$) shown in Fig. 9.

The response dramatically changes for the $n = 3$ iteration order as illustrated in Fig. 10. In this case, a *standing-wave* pattern is clearly visible inside the slab. Looking at the longitudinal cut in Fig. 10(b), from the distance of two consecutive peaks ($\sim 0.241\lambda$), we can estimate a propagation constant $k_x \approx 0.415d/\pi$, which is in excellent agreement with the $k_{x0} = 0.4138d/\pi$ value pertaining to the degenerate additional extraordinary wave predicted by the EFCs in Fig. 2(d) for $k_z = 0$ (normal incidence). The x cut in Fig. 10(c), markedly different from the standard-periodic-multilayer counterparts in Figs. 8(c) and 9(c), shows a transverse field profile with much larger amplitude variations and with peaks at the interfaces

between positive- and negative-permittivity layers, thereby, evidencing the *nonlocal* nature of this mode due to the coupling of SPPs propagating along the interfaces.

Qualitatively similar results can be observed for the higher-order iterations $n = 4$ (Fig. 11) and $n = 5$ (Fig. 12). However, the response in Fig. 12 is more complex than the previous cases since the standing wave inside the slab now results from the interference of three waves (cf. Fig. 5) with different wave numbers. Also, a moderate increase (by a factor of ~ 3) in the peak amplitudes is observed.

The above field maps validate our previous EFC-based studies, demonstrate the actual excitability of the additional extraordinary waves, and provide some useful insight into their physical nature. However, it would be interesting to relate these nonlocal effects to more practically accessible observables and to investigate their sensitivity with respect to the geometrical parameters as well as the unavoidable material dispersion and losses. To this aim, for the same parameter configuration above, Fig. 13 compares the transmittances observed for the $n = 1$ and $n = 3$ iteration orders as a function of the slab thickness at a fixed frequency. For the $n = 1$ iteration order (i.e., standard periodic case), the transmittance exhibits a very fast monotonic decay, whereas, for the $n = 3$ iteration order, we can observe a series of sharp peaks characterized by almost perfect transmission. For this latter case, Fig. 14 shows a more realistic response as a function of the normalized frequency. More specifically, we assume ω_0 as a fiducial angular frequency and consider a Drude-type dispersion model for the negative-permittivity material constituent,

$$\epsilon_b(\omega) = 1 - \frac{\omega_p^2}{\omega(\omega + i\gamma)}, \quad (15)$$

with parameters (given in the caption) chosen so that $\text{Re}[\epsilon_b(\omega_0)] = -1.83$ with a loss tangent of 10^{-3} . We still observe a series of sharp transmittance peaks, although with a reduced dynamic range, due to the various detuning effects as well as the losses.

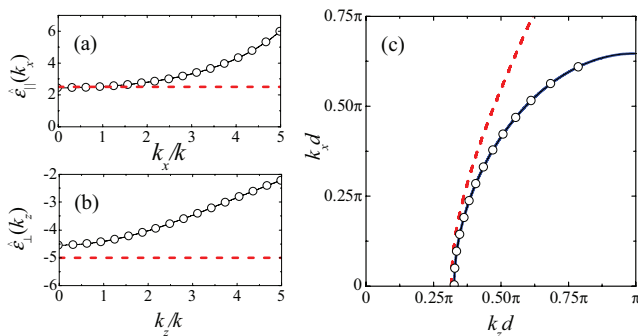


FIG. 6. (Color online) Geometry and parameters as in Fig. 2. (a) and (b) Effective nonlocal relative permittivities $\hat{\epsilon}_\parallel(k_x)$ and $\hat{\epsilon}_\perp(k_z)$ [cf. (13) and Tables I and II], respectively, as a function of the normalized wave numbers for the $n = 1$ iteration order (circles). (c) Corresponding EFC [cf. (12)]. Also shown as references are the local EMT predictions (red-dashed curves) and the exact EFC (blue-solid curve).

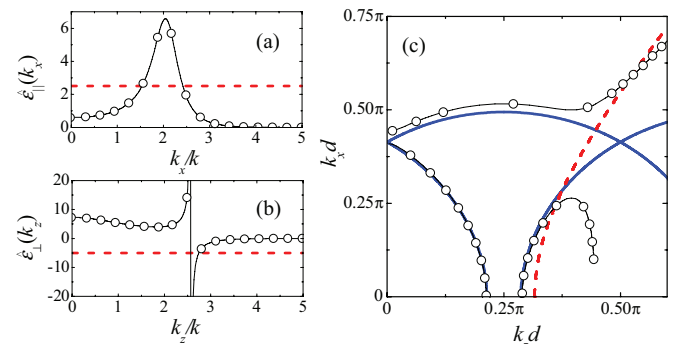


FIG. 7. (Color online) As in Fig. 6 but for the $n = 3$ iteration order.

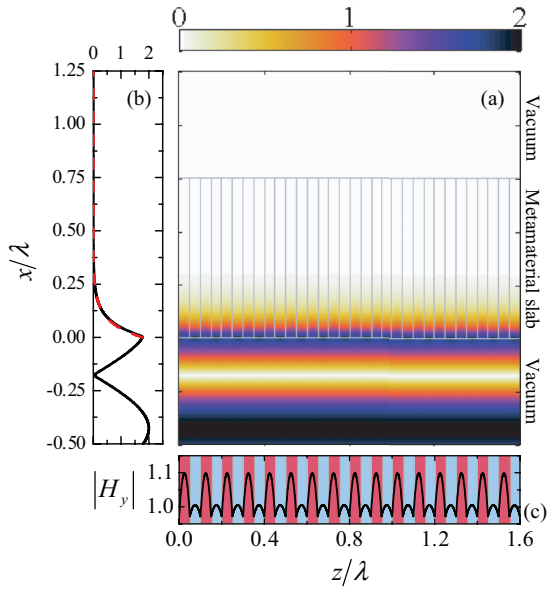


FIG. 8. (Color online) (a) Numerically computed field-magnitude (H_y) map on a false-color scale for a slab of hyperbolic metamaterial (parameters as in Fig. 2) at the $n = 1$ iteration order (standard periodic multilayer of period d ; 16 unit cells shown) of thickness $L = 0.75\lambda$, embedded in vacuum and excited by a unit-amplitude normally incident ($k_z = 0$) plane wave. Thin gray lines delimit the slab and layer interfaces. (b) Longitudinal cut (black-solid curve) at $z = 0.05\lambda$ and exponential fit (red-dashed curve) of the evanescent decay inside the slab as predicted by the local EMT model [cf. (14)]. (c) Transverse cut at $x = 0.05\lambda$ with the material layers visualized with different colors/shades.

As anticipated in Sec. III B, the nonlocal effective parameters in (13) are generally inadequate to provide an accurate description of the slab response. Nevertheless, they can still correctly predict some coarse features. For instance,

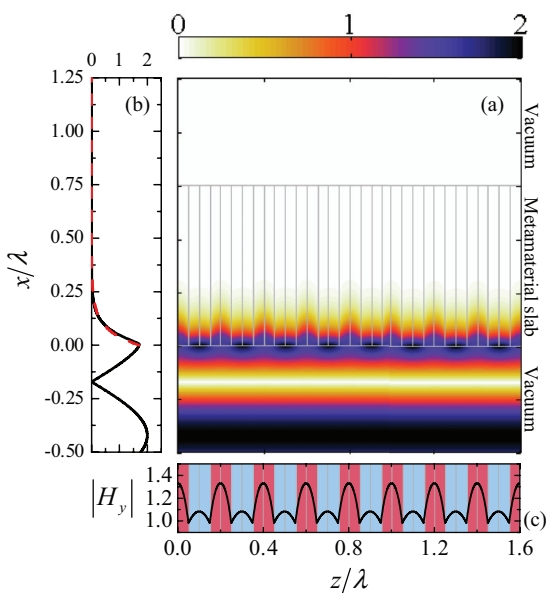


FIG. 9. (Color online) As in Fig. 3 but for the $n = 2$ iteration order (standard periodic multilayer of period $2d$; eight unit cells shown).

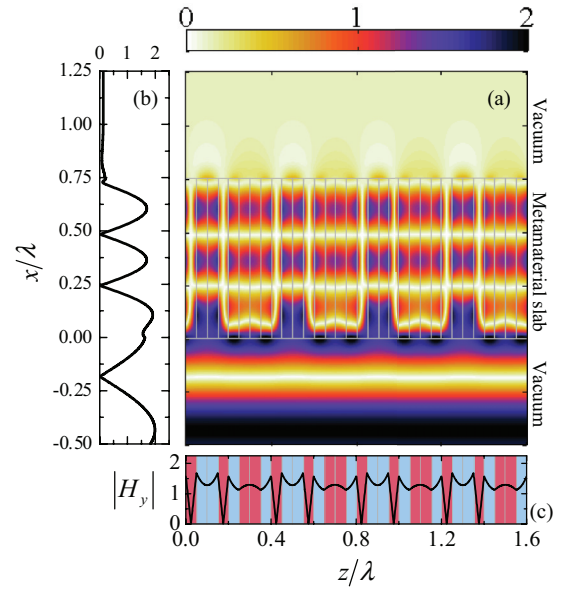


FIG. 10. (Color online) As in Fig. 3 but for the $n = 3$ iteration order (four unit cells shown). Longitudinal and transverse cuts in (b) and (c) are at $z = 0.05\lambda$ and $x = 0.375\lambda$, respectively.

by estimating, via (13), the *effective material wavelength* (for normal incidence, i.e., $k_z = 0$),

$$\lambda_e = \frac{\lambda}{\sqrt{\hat{\epsilon}_\perp(0)}}, \quad (16)$$

as a function of frequency, we observe that the transmittance peaks in Fig. 14 occur at frequencies for which the slab thickness approaches a half-integer number of λ_e (see the inset). Therefore, these peaks are attributable to Fabry-Pérot-type resonances of the additional extraordinary waves.

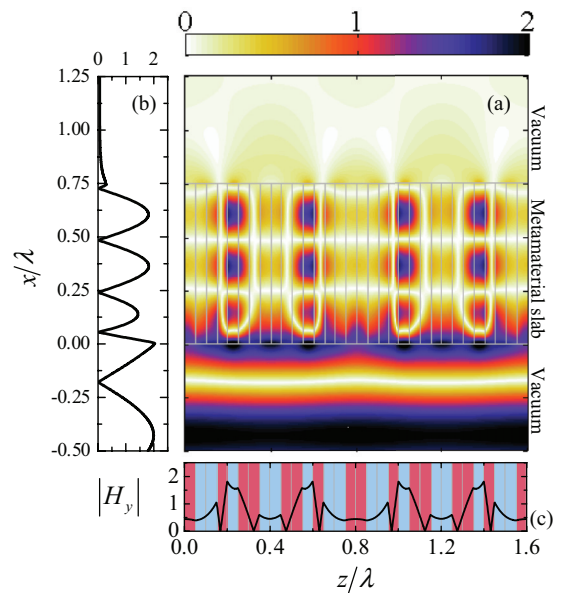


FIG. 11. (Color online) As in Fig. 3 but for the $n = 4$ iteration order (two unit cells shown). Cuts in (b) and (c) are at $z = 0.2\lambda$ and $x = 0.375\lambda$, respectively.

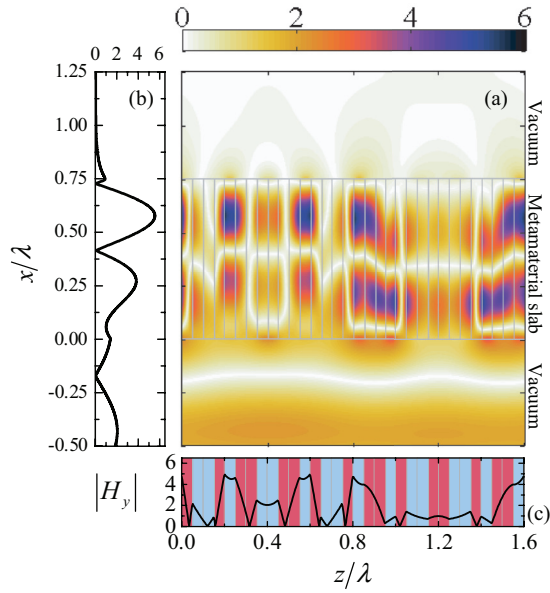


FIG. 12. (Color online) As in Fig. 3 but for the $n = 5$ iteration order (one unit cell shown). Cuts in (b) and (c) are at $z = 0.2\lambda$ and $x = 0.27\lambda$, respectively.

IV. SOME REMARKS

A. The role of aperiodic order

Since the above results refer to various *finite* iteration orders of the ThM geometry, one may wonder to what extent they are attributable to the inherent periodic truncation of the supercell (cf. Fig. 1) or to more or less trivial scaling effects, rather than the actual aperiodic order. The following considerations are in order.

First, we highlight that the particular structure of the ThM inflation rule in (1) ensures that, at any iteration order, no more than two consecutive identical symbols may occur (e.g., *aaa* and *bbb*, or longer, sequences are forbidden).²¹ This implies that the nonlocal effects observed are not trivially attributable to an effective increase in the average layer thickness.

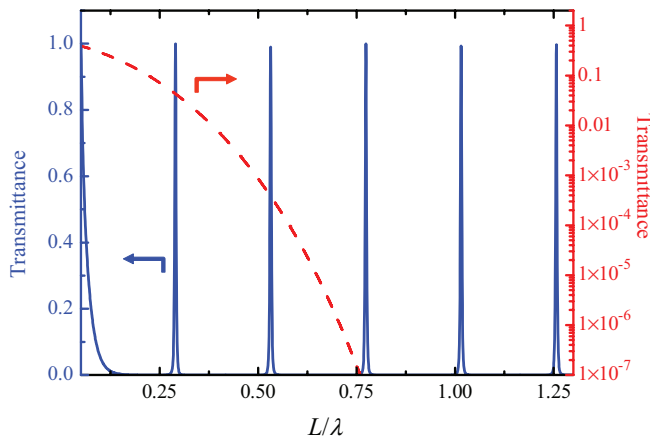


FIG. 13. (Color online) Geometry and parameters as in Figs. 8 and 10. Transmittance as a function of the slab thickness for the $n = 1$ (red-dashed curve; right axis with the logarithmic scale) and $n = 3$ (blue-solid curve; left axis) at a fixed frequency.

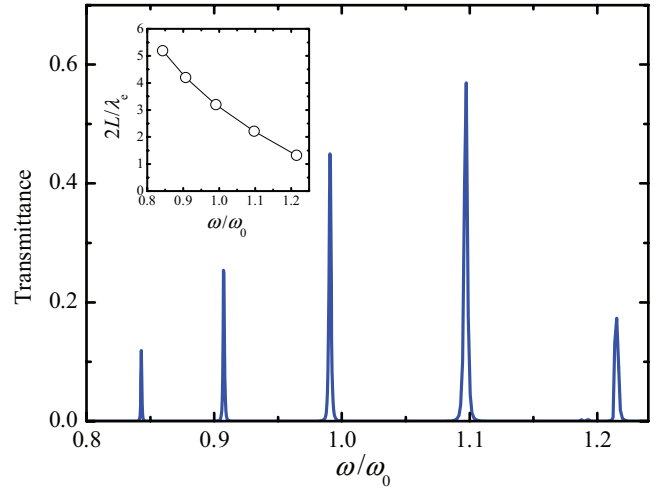


FIG. 14. (Color online) As in Fig. 13 but for fixed slab thickness and the $n = 3$ iteration order as a function of the normalized angular frequency. A fiducial angular frequency ω_0 is assumed (with λ_0 denoting the corresponding wavelength), and the negative-permittivity constituent material is modeled via the Drude-type dispersion law in (15) with $\omega_p = 1.682\omega_0$ and $\gamma = 6.47 \times 10^{-4}\omega_0$ so that so that $\text{Re}[\epsilon_b(\omega_0)] = -1.83$ with a loss tangent of 10^{-3} . The slab and constituent-layer thicknesses are chosen as $L = 0.75\lambda_0$ and $d_a = d_b = d/2 = 0.05\lambda_0$. The inset shows the slab thickness normalized with respect to the effective material (half)wavelength in (16).

Second, we recall that the trace-map formalism may be effectively utilized to infer some *asymptotic* properties in the limit $n \rightarrow \infty$, i.e., in the limit for which the artificial periodicity enforced by the Bloch-type phase-shift walls is washed out by the actual aperiodic order. Within this framework, from Fig. 2, we observe that the stationary point at k_{x0} corresponds to $\chi_3 = 2$, which represents the band-edge condition. When substituted in (10) (together with $\dot{\chi}_3 = 0$), this also implies that $\dot{\chi}_4 = 0$ at k_{x0} . Moreover, we note from the trace map (7) that this will also imply that

$$\chi_n(k_{x0}^2) = 2, \quad \dot{\chi}_n(k_{x0}^2) = 0, \quad n \geq 5. \quad (17)$$

In other words, the additional extraordinary waves associated with the stationary point at k_{x0} will be retained by any arbitrarily high iteration order of the ThM multilayer and, hence, in the actual aperiodic-order limit.

B. Relationship with resonant transmission

In previous papers,^{23,26} the condition $\chi_n = 2$ has also been associated with perfect transmission through ThM-based quasicrystal multilayers. We emphasize that such configurations are, however, different from our slab configurations in Figs. 8–12 since they assume a finite-size (along z) n th-order ThM dielectric multilayer sandwiched between two infinite (along z) homogeneous isotropic media. Conversely, in our configurations in Figs. 8–12, the slab is truncated along the x direction, and the material constituents have oppositely signed permittivities.

For the ThM multilayer configurations as in Refs. 23 and 26, it can be shown that the transmittance pertaining to a generic

iteration order n can be parametrized as²⁹

$$T_n = \frac{4}{\chi_n^2 + v_n^2}, \quad (18)$$

with v_n denoting the “antitrace” (i.e., the difference between the off-diagonal terms M_{21} and M_{12}) of the multilayer transfer matrix \underline{M} (see Appendix A). Interestingly, for the ThM sequence, the antitrace also admits a simple map. In particular, letting v_n and \tilde{v}_n be the transfer-matrix antitraces pertaining to a ThM multilayer at iteration order n initiated by an ab or a “ ba ” sequence, respectively, the following recursive rules hold:²⁹

$$\begin{aligned} v_{n+1} &= \chi_n[(\chi_n - 1)v_n + \tilde{v}_{n-1}], \\ \tilde{v}_{n+1} &= \chi_n[(\chi_n - 1)\tilde{v}_n + v_{n-1}], \quad n \geq 1. \end{aligned} \quad (19)$$

In the lossless case (i.e., real-valued traces and antitraces), we note that the condition $\chi_1 = 0$ (which ensures the presence of additional extraordinary waves in our scenario) also implies $\chi_n = 2, v_n = \tilde{v}_n = 0$, i.e., $T_n = 1$ for $n \geq 3$ in (18). This corresponds to perfect transmission in the scenarios of Refs. 23 and 26. Paralleling those studies and generalizing the underlying approaches (see, e.g., Ref. 26), for our scenario, it can be shown that the number of additional extraordinary waves grows *exponentially* with the iteration order. In particular, the spectrum exhibits self-similarity and characteristic trifurcation.²³

C. The case of $\varepsilon_{\parallel} > 0, \varepsilon_{\perp} < 0$

Although all results above pertain to a parameter configuration featuring $\varepsilon_{\parallel} > 0$ and $\varepsilon_{\perp} < 0$, qualitatively similar considerations also hold for parameter configurations characterized by $\varepsilon_{\parallel} < 0$ and $\varepsilon_{\perp} > 0$.

Figure 15 shows the traces and corresponding EFCs at iteration orders $n = 1$ and $n = 2$ as in Fig. 2 but with different material parameters (given in the caption) corresponding to

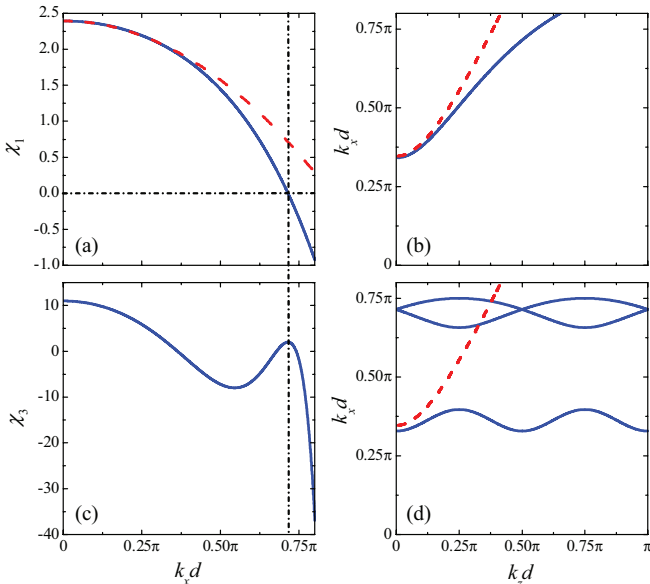


FIG. 15. (Color online) As in Fig. 2 but for $\varepsilon_a = 1, \varepsilon_b = -3$ (i.e., $\varepsilon_{\parallel} = -1, \varepsilon_{\perp} = 3$).

$\varepsilon_{\parallel} = -1$ and $\varepsilon_{\perp} = 3$. Once again, parameters are chosen so that the first iteration $n = 1$ (standard periodic multilayer) is reasonably well described by the local (EMT) model. As can be observed from Fig. 15(a), the trace χ_1 agrees pretty well with its quadratic approximation in (9) up to values of $k_x \lesssim 0.5\pi/d$ and vanishes at $k_{x0} = 0.715\pi/d$. Therefore, by comparison with the case in Fig. 2, the simple analytical approximation in (11) now yields a larger ($\sim 20\%$) error in the position of the zero. Nonetheless, as can be observed from Fig. 15(b), the local EMT model still correctly predicts the presence of a single wave propagating for arbitrarily small values of k_z . As expected, the trace χ_3 , pertaining to the $n = 3$ iteration order, exhibits a maximum ($\chi_3 = 2$) at k_{x0} [see Fig. 15(c)]. However, unlike the case in Fig. 15(c), it now also exhibits a local minimum at $k_x = 0.546\pi/d$, which arises from the vanishing of the term in square brackets in (10). In the corresponding EFCs, this yields [Fig. 15(d)] *three* (always propagating) modes, one of which approaches the local EMT prediction for small values of k_z . The other two, instead, represent additional extraordinary waves which degenerate at $k_z^{(m)} = m\pi/(2d), m = 0, 1, 2, \dots$. Therefore, the same general observations and conclusions hold as for the case featuring $\varepsilon_{\parallel} > 0$ and $\varepsilon_{\perp} < 0$ in Fig. 2. However, the field distributions for plane-wave-excited slab configurations (not shown for brevity) are less clean cut than those in Figs. 8 and 10 since the local mode is now always propagating, and thus, the difference between the standard periodic multilayer and the $n = 3$ iteration order is less striking.

V. CONCLUSIONS

To sum up, we have shown that hyperbolic metamaterials, implemented as multilayered based on the ThM sequence, may exhibit strong optical nonlocality, manifested as the appearance of additional extraordinary waves and a strong wave-vector dependence in the effective constitutive parameters. From the mathematical viewpoint, we associated these effects with stationary points of the transfer-matrix trace and derived simple analytical design rules. The chosen ThM geometry is particularly interesting since different iteration orders differ solely in the positional order of the constituent material layers. Interestingly, we identified some configurations for which these nonlocal effects are rather weak at the first two iteration orders ($n = 1, 2$, corresponding to standard periodic multilayers) and become markedly more prominent at higher iteration orders $n \geq 3$, even in the limit $n \rightarrow \infty$ for which the (periodic) truncation effects become progressively less relevant.

To the best of our knowledge, against the many implications and applications of aperiodic order to optics and photonics (see, e.g., Refs. 32 and 33 for recent reviews), this represents evidence in connection with optical nonlocality. Besides the inherent academic interest, from the application viewpoint, this constitutes an important and technologically inexpensive additional degree of freedom in the engineering of optical nonlocality, which may also be fruitfully exploited within the recently introduced framework of nonlocal transformation optics.³⁴

We highlight that the ThM sequence was considered here only in view of its particularly simple inflation rule and

associated trace map, which facilitate analytical treatment as well as direct comparison with standard periodic multilayers, but the results are more general. In fact, one of the most intriguing follow-up studies may be the systematic design of deterministic aperiodic sequences via suitable inflation rules and associated polynomial trace maps,²⁸ yielding prescribed nonlocal effects.

APPENDIX A: DISPERSION RELATIONSHIPS FOR GENERIC MULTILAYERS

The dispersion relationship of a periodic multilayer consisting of the infinite replication of a generic supercell can be straightforwardly obtained by applying the rigorous transfer-matrix approach.³⁵ Figure 16 schematically illustrates a rather general supercell composed of N layers with relative permittivity ε_j and thickness $d_j, j = 1, \dots, N$, stacked along the z direction. For the assumed TM polarization, the tangential components at the two interfaces of a generic j th layer can be related as

$$\begin{bmatrix} E_x^{(j)} \\ i\eta H_y^{(j)} \end{bmatrix} = \underline{\underline{M}}^{(j)} \cdot \begin{bmatrix} E_x^{(j+1)} \\ i\eta H_y^{(j+1)} \end{bmatrix}, \quad (\text{A1})$$

where η denotes the vacuum characteristic impedance, the (x, z) dependence in the fields has been omitted for notational compactness, and the *unimodular* transfer matrix is given by

$$\underline{\underline{M}}^{(j)} = \begin{bmatrix} \cos \delta_j & -\frac{\sin \delta_j}{\gamma_j} \\ \gamma_j \sin \delta_j & \cos \delta_j \end{bmatrix}, \quad (\text{A2})$$

with

$$\delta_j = k_{zj} d_j, \quad \gamma_j = \frac{\varepsilon_j k}{k_{zj}}, \quad k_{zj} = \sqrt{k^2 \varepsilon_j - k_x^2}, \quad \text{Im}(k_{zj}) \geq 0, \quad (\text{A3})$$

and k_x indicating the (conserved) transverse wave number. Proceeding layer by layer, the tangential field components at

the interfaces of the supercell can be, therefore, related by cascading the relevant transfer matrices, viz.,

$$\begin{bmatrix} E_x^{(1)} \\ i\eta H_y^{(1)} \end{bmatrix} = \underline{\underline{M}} \cdot \begin{bmatrix} E_x^{(N+1)} \\ i\eta H_y^{(N+1)} \end{bmatrix}, \quad (\text{A4})$$

with

$$\underline{\underline{M}} = \prod_{j=1}^N \underline{\underline{M}}^{(j)} = \begin{bmatrix} M_{11} & M_{12} \\ M_{21} & M_{22} \end{bmatrix}. \quad (\text{A5})$$

In view of the assumed overall periodicity along z , the fields should likewise be periodic of period L (the overall thickness of the supercell), apart from a phase factor. This can be enforced via Bloch-type phase-shift conditions at the supercell interfaces $z = 0$ and $z = L$,

$$\begin{bmatrix} E_x^{(1)} \\ i\eta H_y^{(1)} \end{bmatrix} = \exp(-ik_{zB}L) \begin{bmatrix} E_x^{(N+1)} \\ i\eta H_y^{(N+1)} \end{bmatrix}, \quad (\text{A6})$$

with k_{zB} denoting the Bloch propagation constant. The arising homogeneous linear system of equations admits nontrivial solutions if

$$\det[\underline{\underline{M}} - \exp(-ik_{zB}L)\underline{\underline{I}}] = 0, \quad (\text{A7})$$

with $\underline{\underline{I}}$ denoting the 2×2 identity matrix. Recalling that the supercell transfer matrix $\underline{\underline{M}}$ in (A5) is unimodular (as the product of unimodular matrices), i.e.,

$$\det(\underline{\underline{M}}) = M_{11}M_{22} - M_{12}M_{21} = 1, \quad (\text{A8})$$

the relationship in (A6) can be recast as

$$\cos(k_{zB}L) = \frac{1}{2}(M_{11} + M_{22}) = \frac{1}{2}\text{Tr}(\underline{\underline{M}}), \quad (\text{A9})$$

with Tr denoting the *trace* operator.³⁶

APPENDIX B: TRACE MAP FOR THUE-MORSE SUPERLATTICES

For a multilayer composed of only two types of layers (labeled a and b) arranged according to the ThM aperiodic sequence of interest in our study, the trace of the supercell transfer matrix at a generic iteration order n need not be calculated via the product in (A5) but can be obtained in a much more direct fashion via the trace-map formalism.^{28,29} Letting $\underline{\underline{M}}_n$ and $\tilde{\underline{\underline{M}}}_n$ be the transfer matrices pertaining to a ThM multilayer at iteration order n initiated by an ab -type or a ba -type sequence, respectively, the following recursive rules hold:²⁵

$$\underline{\underline{M}}_{n+1} = \underline{\underline{M}}_n \cdot \tilde{\underline{\underline{M}}}_n, \quad \tilde{\underline{\underline{M}}}_{n+1} = \tilde{\underline{\underline{M}}}_n \cdot \underline{\underline{M}}_n, \quad (\text{B1})$$

with initial conditions,

$$\underline{\underline{M}}_0 = \underline{\underline{M}}^{(a)}, \quad \tilde{\underline{\underline{M}}}_0 = \underline{\underline{M}}^{(b)}, \quad (\text{B2})$$

where $\underline{\underline{M}}^{(a)}$ and $\underline{\underline{M}}^{(b)}$ denote the transfer matrices associated with a single a -type and b -type layer, respectively. These latter may formally be obtained via (A1)–(A3) by replacing the layer index j with the symbols a and b , respectively. Thus, for a

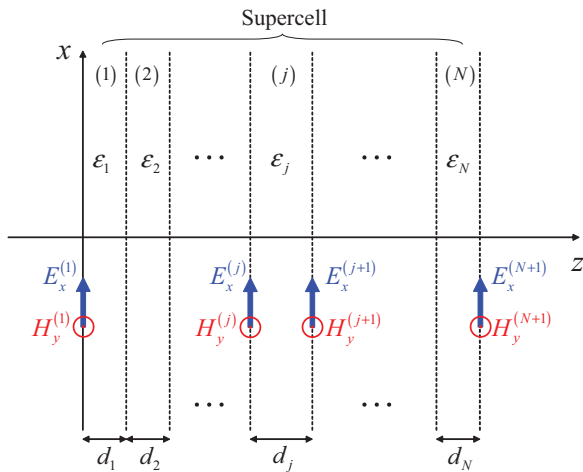


FIG. 16. (Color online) Geometry of a general supercell composed of N layers with relative permittivities ε_j and thicknesses $d_j, j = 1, \dots, N$ stacked along the z direction. Also shown are the tangential field components $E_x^{(j)}$ and $H_y^{(j)}$ at the layer interfaces, relevant for TM polarization.

given iteration order $n \geq 1$, we obtain

$$\begin{aligned}\chi_n &\equiv \text{Tr}(\underline{\underline{M}}_n) = \text{Tr}(\underline{\underline{M}}_{n-1} \cdot \underline{\underline{\tilde{M}}}_{n-1}) \\ &= \text{Tr}(\underline{\underline{\tilde{M}}}_{n-1} \cdot \underline{\underline{M}}_{n-1}) = \text{Tr}(\underline{\underline{\tilde{M}}}_n),\end{aligned}\quad (\text{B3})$$

whereas, for adjacent iteration orders, we can write

$$\begin{aligned}\chi_{n+2} &= \text{Tr}(\underline{\underline{M}}_{n+2}) = \text{Tr}(\underline{\underline{M}}_{n+1} \cdot \underline{\underline{\tilde{M}}}_{n+1}) \\ &= \text{Tr}(\underline{\underline{M}}_n \cdot \underline{\underline{\tilde{M}}}_n \cdot \underline{\underline{\tilde{M}}}_n \cdot \underline{\underline{M}}_n) \\ &= \text{Tr}[(\underline{\underline{M}}_n)^2 \cdot (\underline{\underline{\tilde{M}}}_n)^2], \quad n \geq 1,\end{aligned}\quad (\text{B4})$$

with the last equality following from the trace invariance under cyclic permutations.³⁶ Recalling that, as a consequence of the

Caley-Hamilton theorem,³⁶ the square of a general unimodular matrix $\underline{\underline{A}}$ of trace χ_A can be written as

$$\underline{\underline{A}}^2 = \chi_A \underline{\underline{A}} - \underline{\underline{I}}, \quad (\text{B5})$$

and substituting in (B4), we obtain

$$\begin{aligned}\chi_{n+2} &= \text{Tr}[(\chi_n \underline{\underline{M}}_n - \underline{\underline{I}}) \cdot (\chi_n \underline{\underline{\tilde{M}}}_n - \underline{\underline{I}})] \\ &= \text{Tr}(\chi_n^2 \underline{\underline{M}}_n \cdot \underline{\underline{\tilde{M}}}_n - \chi_n \underline{\underline{M}}_n - \chi_n \underline{\underline{\tilde{M}}}_n + \underline{\underline{I}}) \\ &= \chi_n^2 (\chi_{n+1} - 2) + 2, \quad n \geq 1,\end{aligned}\quad (\text{B6})$$

where, in the last equality, the linearity of the trace operator has been exploited as well as the result in (B3). This yields the trace map in (7).

*vgaldi@unisannio.it

¹F. Capolino, *Metamaterials Handbook* (CRC, Boca Raton, FL, 2009), Vols. 1 and 2.

²D. R. Smith, P. Kolinko, and D. Schurig, *J. Opt. Soc. Am. B* **21**, 1032 (2004).

³M. A. Noginov, Y. A. Barnakov, G. Zhu, T. Tumkur, H. Li, and E. E. Narimanov, *Appl. Phys. Lett.* **94**, 151105 (2009).

⁴Z. Jacob, L. V. Alekseyev, and E. Narimanov, *Opt. Express* **14**, 8247 (2006).

⁵A. A. Govyadinov and V. A. Podolskiy, *Phys. Rev. B* **73**, 155108 (2006).

⁶I. I. Smolyaninov and E. E. Narimanov, *Phys. Rev. Lett.* **105**, 067402 (2010).

⁷Z. Jacob, J.-Y. Kim, G. Naik, A. Boltasseva, E. Narimanov, and V. Shalaev, *Appl. Phys. B* **100**, 215 (2010).

⁸J. Yao, X. Yang, X. Yin, G. Bartal, and X. Zhang, *Proc. Natl. Acad. Sci. USA* **108**, 11327 (2011).

⁹H. N. S. Krishnamoorthy, Z. Jacob, E. Narimanov, I. Kretzschmar, and V. M. Menon, *Science* **336**, 205 (2012).

¹⁰Z. Jacob, I. I. Smolyaninov, and E. E. Narimanov, *Appl. Phys. Lett.* **100**, 181105 (2012).

¹¹C. L. Cortes, W. Newman, S. Molesky, and Z. Jacob, *J. Opt.* **14**, 063001 (2012).

¹²S.-A. Biehs, M. Tschikin, and P. Ben-Abdallah, *Phys. Rev. Lett.* **109**, 104301 (2012).

¹³A. Sihvola, *Electromagnetic Mixing Formulas and Applications* (IEE, London, 1999).

¹⁴J. Elser, V. A. Podolskiy, I. Salakhutdinov, and I. Avrutsky, *Appl. Phys. Lett.* **90**, 191109 (2007).

¹⁵A. A. Orlov, P. M. Voroshilov, P. A. Belov, and Y. S. Kivshar, *Phys. Rev. B* **84**, 045424 (2011).

¹⁶A. V. Chebykin, A. A. Orlov, C. R. Simovski, Y. S. Kivshar, and P. A. Belov, *Phys. Rev. B* **86**, 115420 (2012).

¹⁷O. Kidwai, S. V. Zhukovsky, and J. E. Sipe, *Phys. Rev. A* **85**, 053842 (2012).

¹⁸A. Orlov, I. Iorsh, P. Belov, and Y. Kivshar, *Opt. Express* **21**, 1593 (2013).

¹⁹D. Shechtman, I. Blech, D. Gratias, and J. W. Cahn, *Phys. Rev. Lett.* **53**, 1951 (1984).

²⁰D. Levine and P. J. Steinhardt, *Phys. Rev. Lett.* **53**, 2477 (1984).

²¹M. Queffélec, in *Substitution Dynamical Systems—Spectral Analysis*, Lecture Notes in Mathematics (Springer-Verlag, Berlin/Heidelberg, 2010).

²²N.-H. Liu, *Phys. Rev. B* **55**, 3543 (1997).

²³F. Qiu, R. W. Peng, X. Q. Huang, Y. M. Liu, M. Wang, A. Hu, and S. S. Jiang, *Europhys. Lett.* **63**, 853 (2003).

²⁴L. Dal Negro, M. Stolfi, Y. Yi, J. Michel, X. Duan, L. C. Kimerling, J. LeBlanc, and J. Haavisto, *Appl. Phys. Lett.* **84**, 5186 (2004).

²⁵V. Grigoriev and F. Biancalana, *Photonics Nanostruct. Fundam. Appl.* **8**, 285 (2010).

²⁶W. J. Hsueh, S. J. Wun, Z. J. Lin, and Y. H. Cheng, *J. Opt. Soc. Am. B* **28**, 2584 (2011).

²⁷X. Jiang, Y. Zhang, S. Feng, K. C. Huang, Y. Yi, and J. D. Joannopoulos, *Appl. Phys. Lett.* **86**, 201110 (2005).

²⁸M. Kolář and F. Nori, *Phys. Rev. B* **42**, 1062 (1990).

²⁹X. Wang, U. Grimm, and M. Schreiber, *Phys. Rev. B* **62**, 14020 (2000).

³⁰S. I. Maslovski, T. A. Morgado, M. G. Silveirinha, C. S. R. Kaipa, and A. B. Yakovlev, *New J. Phys.* **12**, 113047 (2010).

³¹M. G. Moharam, E. B. Grann, D. A. Pommet, and T. K. Gaylord, *J. Opt. Soc. Am. A* **12**, 1068 (1995).

³²E. Maciá, *Rep. Prog. Phys.* **69**, 397 (2006).

³³L. Dal Negro and S. Boriskina, *Laser Photonics Rev.* **6**, 178 (2012).

³⁴G. Castaldi, V. Galdi, A. Alù, and N. Engheta, *Phys. Rev. Lett.* **108**, 063902 (2012).

³⁵M. Born and E. Wolf, *Principles of Optics*, 7th ed. (Cambridge University Press, Cambridge, UK, 1999).

³⁶S. Lang, *Linear Algebra*, 3rd. ed. (Springer, Berlin, 1987).